UC Santa Barbara

UC Santa Barbara Previously Published Works

Title

Maximum likelihood analysis of low energy CDMS II germanium data

Permalink

https://escholarship.org/uc/item/2pf4j9rn

Journal

Physical Review D, 91(5)

ISSN

2470-0010

Authors

Agnese, R

Anderson, AJ

Balakishiyeva, D

et al.

Publication Date

2015-03-01

DOI

10.1103/physrevd.91.052021

Peer reviewed

eScholarship.org Powered by the California Digital Library
University of California

Maximum likelihood analysis of low energy CDMS II germanium data

R. Agnese,[19] A. J. Anderson,[4] D. Balakishiyeva,[19] R. Basu Thakur,[2,20] D. A. Bauer,[2] J. Billard,[4] A. Borgland,[9] M. A. Bowles,[12] D. Brandt,[9] P. L. Brink,[9] R. Bunker,[12] B. Cabrera,[11] D. O. Caldwell,[16] D. G. Cerdeno,[14] H. Chagani,[21] Y. Chen,[12] J. Cooley,[10] B. Cornell,[1] C. H. Crewdson,[7] P. Cushman,[21] M. Daal,[15] P. C. F. Di Stefano,[7] T. Doughty,[15] L. Esteban,[14] S. Fallows,[21] E. Figueroa-Feliciano,[4] M. Fritts,[21] G. L. Godfrey,[9] S. R. Golwala,[1] M. Graham,[9] J. Hall,[5] H. R. Harris,[13] S. A. Hertel,[4] T. Hofer,[21] D. Holmgren,[2] L. Hsu,[2] M. E. Huber,[17] A. Jastram,[13] O. Kamaev,[7] B. Kara,[10] M. H. Kelsey,[9] A. Kennedy,[21] M. Kiveni,[12] K. Koch,[21] A. Leder,[4] B. Loer,[2] E. Lopez Asamar,[14] R. Mahapatra,[13] V. Mandic,[21] C. Martinez,[7] K. A. McCarthy,[4] N. Mirabolfathi,[13] R. A. Moffatt,[11] D. C. Moore,[1] R. H. Nelson,[1] S. M. Oser,[6] K. Page,[7] W. A. Page,[6] R. Partridge,[9] M. Pepin,[21] A. Phipps,[15] K. Prasad,[13] M. Pyle,[15] H. Qiu,[10] W. Rau,[7] P. Redl,[11,*] A. Reisetter,[18] Y. Ricci,[7] H. E. Rogers,[21] T. Saab,[19] B. Sadoulet,[15,3] J. Sander,[22] K. Schneck,[9] R. W. Schnee,[12] S. Scorza,[10] B. Serfass,[15] B. Shank,[11] D. Speller,[15] S. Upadhyayula,[13] A. N. Villano,[21] B. Welliver,[19] D. H. Wright,[9] S. Yellin,[11] J. J. Yen,[11] B. A. Young,[8] and J. Zhang[21]

(SuperCDMS Collaboration)

[1]*Division of Physics, Mathematics, and Astronomy, California Institute of Technology, Pasadena, California 91125, USA*
[2]*Fermi National Accelerator Laboratory, Batavia, Illinois 60510, USA*
[3]*Lawrence Berkeley National Laboratory, Berkeley, California 94720, USA*
[4]*Department of Physics, Massachusetts Institute of Technology, Cambridge, Massachusetts 02139, USA*
[5]*Pacific Northwest National Laboratory, Richland, Washington 99352, USA*
[6]*Department of Physics and Astronomy, University of British Columbia, Vancouver, British Columbia V6T 1Z1, Canada*
[7]*Department of Physics, Queen's University, Kingston, Ontario K7L 3N6, Canada*
[8]*Department of Physics, Santa Clara University, Santa Clara, California 95053, USA*
[9]*SLAC National Accelerator Laboratory/Kavli Institute for Particle Astrophysics and Cosmology, 2575 Sand Hill Road, Menlo Park, California 94025, USA*
[10]*Department of Physics, Southern Methodist University, Dallas, Texas 75275, USA*
[11]*Department of Physics, Stanford University, Stanford, California 94305, USA*
[12]*Department of Physics, Syracuse University, Syracuse, New York 13244, USA*
[13]*Department of Physics, Texas A&M University, College Station, Texas 77843, USA*
[14]*Departamento de Física Teórica and Instituto de Física Teórica UAM/CSIC, Universidad Autónoma de Madrid, 28049 Madrid, Spain*
[15]*Department of Physics, University of California, Berkeley, California 94720, USA*
[16]*Department of Physics, University of California, Santa Barbara, California 93106, USA*
[17]*Department of Physics, University of Colorado Denver, Denver, Colorado 80217, USA*
[18]*Department of Physics, University of Evansville, Evansville, Indiana 47722, USA*
[19]*Department of Physics, University of Florida, Gainesville, Florida 32611, USA*
[20]*Department of Physics, University of Illinois at Urbana-Champaign, Urbana, Illinois 61801, USA*
[21]*School of Physics and Astronomy, University of Minnesota, Minneapolis, Minnesota 55455, USA*
[22]*Department of Physics, University of South Dakota, Vermillion, South Dakota 57069, USA*

(Received 10 October 2014; published 30 March 2015)

We report on the results of a search for a Weakly Interacting Massive Particle (WIMP) signal in low-energy data of the Cryogenic Dark Matter Search experiment using a maximum likelihood analysis. A background model is constructed using GEANT4 to simulate the surface-event background from ^{210}Pb decay-chain events, while using independent calibration data to model the gamma background. Fitting this background model to the data results in no statistically significant WIMP component. In addition, we perform fits using an analytic *ad hoc* background model proposed by Collar and Fields, who claimed to find a large excess of signal-like events in our data. We confirm the strong preference for a signal hypothesis in their analysis under these assumptions, but excesses are observed in both single- and multiple-scatter events, which implies the signal is not caused by WIMPs, but rather reflects the inadequacy of their background model.

DOI: 10.1103/PhysRevD.91.052021 PACS numbers: 95.35.+d, 85.30.-z, 95.30.Cq, 29.40.Wk

*redl@stanford.edu

 © 2015 American Physical Society

I. INTRODUCTION

The existence of dark matter has been confirmed through astrophysical observations, most recently from the Planck Collaboration finding that 27% of the Universe consists of cold dark matter [1]. Weakly Interacting Massive Particles (WIMPs) [2] are a favored candidate to explain the dark matter. These might interact with normal matter by elastically scattering from nuclei, but the scattering rates and WIMP masses are unknown. To detect the nuclear recoil signals caused by WIMP scatters in terrestrial detectors, interactions with normal matter that might mimic such signals must be eliminated, or at least accurately modeled. Great care has been taken in the Cryogenic Dark Matter Search experiment (CDMS II) to reduce the number of neutrons that would give nuclear recoil signals; less than 1 neutron-induced nuclear recoil is expected in the full data set. The dominant backgrounds arise from residual radioactivity in the materials used to construct the structures around the detectors; the decay products are typically photons causing electron recoil events.

CDMS II [3,4] cooled germanium and silicon detectors to temperatures of $\lesssim$50 mK in order to detect ionization and athermal phonons ("heat") generated by the elastic scattering of WIMPs from nuclei. Nuclear recoil (NR) events produce less ionization compared to similar energy electron recoil (ER) events. Consequently, NR and ER events can be separated. However, at recoil energies $\lesssim$10 keVnr (nuclear recoil equivalent energy, see Fig. 1), background events start populating the signal region. This figure shows calibration data for both ^{133}Ba (a gamma source) and ^{252}Cf (a neutron source). At energies above

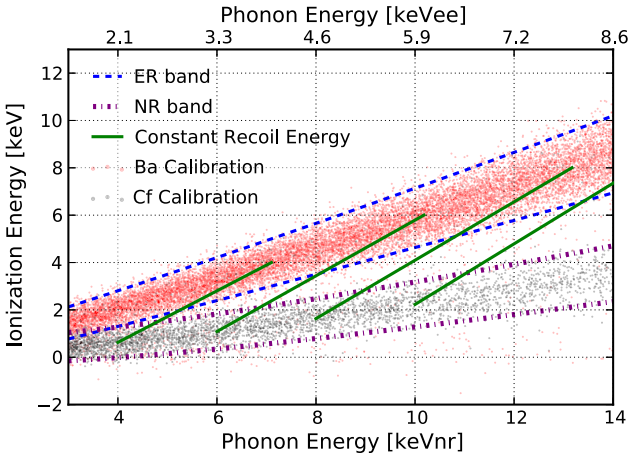

FIG. 1 (color online). Events in the ionization- versus recoil-energy plane for one detector. Events from ^{133}Ba and ^{252}Cf calibration data are shown. The recoil-energy scale is given by the total phonon energy minus the Neganov-Luke phonon [5] contribution. The keVnr scale (bottom x axis) gives the correct recoil energy at the center of the NR band, while the keVee scale (top x axis) gives the correct recoil energy at the center of the ER band.

$\sim$10 keVnr there is good separation between gamma and neutron events. However, at lower energies the apparent bands of nuclear and electron recoils (NR and ER "bands") start to merge. At low energies a likelihood analysis can exploit the different distributions of signal and background in this two-dimensional space to search for a WIMP signal. We show that while this is a powerful technique, it requires a trustworthy background model. Producing such a model can be a challenging task.

Recent results from DAMA [6], CoGeNT [7] and CDMS II Si [8] can be interpreted as signals from 5–15 GeV/c^2 WIMPs, but results from CDMS II Ge [9], SuperCDMS [10] and LUX [11] are in tension with these interpretations. Collar and Fields [12] claimed evidence for a WIMP-like signal in CDMS II data after attempting to estimate and effectively subtract the background. We investigate that claim with a careful study of the backgrounds, thereby permitting an improved background modeling. We present a maximum likelihood (ML) analysis of data from CDMS II's germanium detectors from 3–14 keVnr, taken between 2006 and 2008. Details of the detectors are given in Sec. II. We estimate background distributions using identified sources of background, either by simulating their detector response or by using a representative calibration sample. A detailed description of the background model is provided in Sec. III and its implementation in the ML analysis is discussed in Sec. IV. In Sec. V we study systematic effects before presenting the results in Sec. VI.

In addition, we present a ML fit to these data using *ad hoc* analytic models for background and signal. We use the functional forms proposed by Collar and Fields [12], whose fit to these data show a strong preference (5.7σ C.L.) for a model containing an exponentially falling excess of events at low recoil energy in the NR band, consistent with a low-mass WIMP hypothesis. We also find a strong preference for a WIMP-like signal under the given assumptions. In Sec. VII we show evidence that this is a consequence of the inadequacy of the background model.

For both types of ML analyses, we separately fit samples of events with energy deposited in only one detector ("single scatters" or "singles") as well as samples of events with simultaneous energy depositions in multiple detectors ("multiple scatters" or "multiples"). A WIMP signal is not expected in the multiples data. Therefore, a signal preference in the multiples data suggests that a similar excess in the singles data is likely caused by an incomplete or incorrect modeling of the backgrounds.

II. CDMS II DETECTORS

CDMS II used a mix of Ge and Si detectors, each $\sim$100 mm thick and 76 mm in diameter. They were packaged in copper housings that were stacked to form towers of six detectors each. Here we chose to analyze the four Ge detectors, out of 30 total (19 Ge and 11 Si), that had the most favorable electronic noise characteristics as well

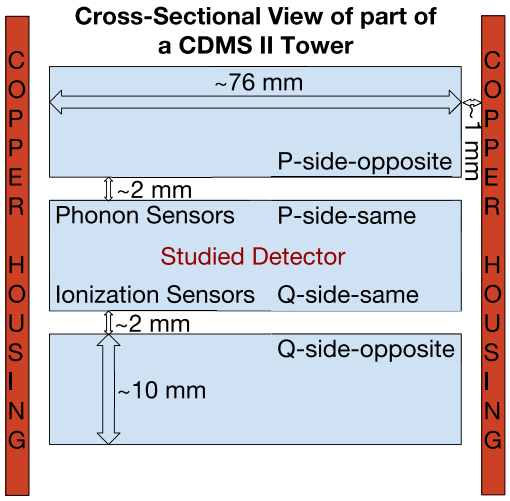

FIG. 2 (color online). A simple detector schematic (not to scale), showing an analyzed detector in the center along with the two neighboring detectors. The detectors are surrounded by copper housings. Detectors had phonon sensors on their top surfaces and ionization sensors on the bottom. Surface events originating from decays on the "studied detector" are named "P-side-same" or "Q-side-same" depending on whether the decay occurred on the phonon or ionization side. In simulations, surface events (SEs) on the studied detector that originate from a decay on a detector adjacent to the studied detector are either named "P-side-opposite" or "Q-side-opposite" depending on whether the decay caused an energy deposition on the phonon or ionization side of the studied detector.

as the lowest-energy thresholds. The detectors chosen for this study are denoted T1Z1, T1Z5, T2Z5, and T3Z4, with "T" indicating the tower number (1–5) and "Z" indicating the detector number in the tower (1–6 from top to bottom).

The CDMS II detectors were instrumented with phonon sensors on one surface and ionization sensors on the other surface, while the sidewalls of the cylindrical detectors were not instrumented. The ionization side had a central circular electrode and an outer guard ring that allowed differentiation of interactions near the sidewall from those in the crystal interior. A simple schematic of a detector is shown in Fig. 2. Simultaneous measurement of phonon and ionization signals enabled discrimination of NR and ER events via construction of the ratio of ionization to phonon energy ("ionization yield"). Events near a surface (depth $<$ few μm) can have diminished ionization yield, and thus ER events can leak into the NR signal region. Events near the surfaces are referred to as surface events, while events away from the surfaces are referred to as bulk events. More details of the CDMS II detectors can be found in [3,4].

III. THE BACKGROUND MODEL

The CDMS II detectors were shielded from external backgrounds with layers of copper, lead and polyethylene. Furthermore, to decrease the background from neutrons produced by cosmic rays, the experiment was located 2090 meters water equivalent underground at the Soudan Underground Laboratory and surrounded by a muon veto detector. However, the detectors are not background-free for the lowest-energy recoils considered here. In particular, we consider two types of ER background: the "gamma background" and the "surface-event background." The former results from scatters of gamma rays throughout the detector and enters the low-energy signal region where finite energy resolution causes the ER and NR bands to overlap. The surface-event background is due to events near the detector faces and sidewalls that have incomplete charge collection, resulting in degraded ionization yield that leads to misidentification as NR events. The neutron background is very low ($<$1 event in this data set) and is therefore ignored.

A. The gamma background

All materials contain radioactive contaminants. Thus, although care was taken to minimize radio contamination in the construction of the CDMS II cryostat, support structures, detectors housings, and the detectors themselves, each component contains some contamination. The majority of the gamma background observed in CDMS II is caused by decays from radioactive U, Th (and their decay-chain daughters) and ^{40}K occurring in the surrounding materials. Additionally, Ge has radioactive isotopes that can be produced by neutrons or cosmogenic radiation (^{68}Ge and ^{71}Ge). These isotopes decay via electron capture producing characteristic lines at 10.4 keVee (K-shell) and 1.3 keVee (L-shell). We chose our analysis energy range of 3–14 keVnr to avoid these activation lines. Figure 3 shows the gamma background for a recoil energy up to 30 keVnr for both single and multiple scatters, with the K-shell activation peak clearly visible at ~17 keVnr (10.4 keVee) in the single-scatter data. Other low-energy electron recoils

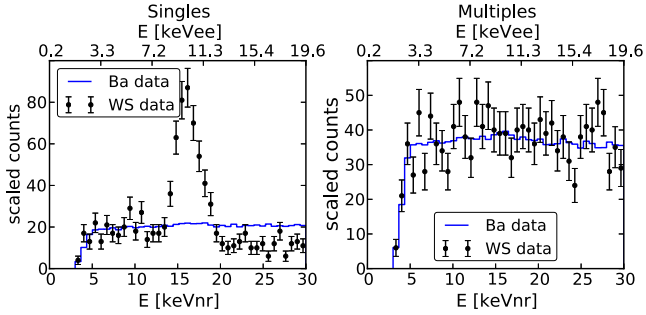

FIG. 3 (color online). WS data and Ba calibration data for events within the ER band for detector T1Z2, given in NR (ER) equivalent phonon energy along the bottom (top) axis. The 10.4 keVee (17 keVnr) Ge activation line is clearly seen in the single-scatter WIMP-search data (left panel) but absent in the Ba calibration and multiple-scatter WIMP-search data (right panel).

(or "gammas") result from a variety of sources, including cosmogenic activation of non-Ge isotopes and small-angle Compton scattering.

B. The gamma-background model

Bulk gamma events are modeled using ^{133}Ba calibration data. Although dominated by a line at 356 keVee, sufficient Compton scattering occurs throughout the surrounding mechanical structures that a flat recoil spectrum is observed between 3 and 14 keVnr (see Fig. 4). Ba calibration data runs were interspersed with WIMP-search (WS) data runs, where the latter are defined as all data taken without a calibration source. Two Ba sources were inserted through special tubes that went through the lead shield. Placing the sources inside the lead shield increases the number of events collected and allows the 356 keVee line to be resolved. This line was used to calibrate the electron recoil-energy scale. One source was located below the detectors, while the other source was located above. The two source configuration leads to a more homogeneous distribution of events among the detectors. While the sources were pushed all the way through the lead shield, gammas from the sources still had to travel through several centimeters of Cu to get to a detector and through some Ge for the inner detectors. Additional information on the calibration sources can be found in [13].

For the analysis presented here, Ba calibration data are a good proxy for WIMP-search gamma events if the energy spectrum of WIMP-search and barium calibration events are the same in the energy region of interest. Figure 4 shows a comparison between the energy spectrum of barium and WIMP-search events in the ER band. Kolmogorov-Smirnov (KS) tests [14] comparing the two distributions between 3 and 14 keVnr indicate that their shapes are compatible. The individual detectors T1Z2, T1Z5, T2Z5 and T3Z4 have KS p-values of 0.8 (0.5), 0.7 (0.2), 0.07 (0.8), and 0.013 (0.8) for multiples (singles), respectively.

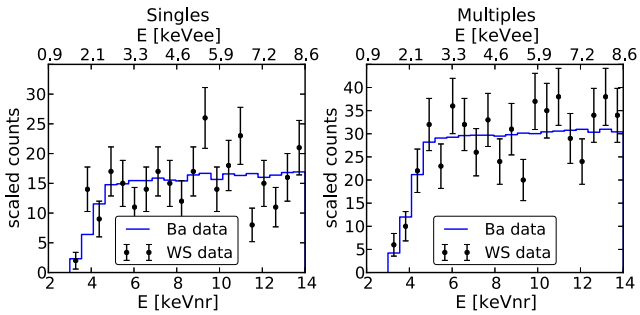

FIG. 4 (color online). Phonon energy spectra comparison of events in the ER band. The singles spectrum is shown in the left panel while the multiples spectrum is shown in the right panel. Ba calibration and WS data are well matched. The p-value from a Kolmogorov-Smirnov test for the detector shown (T1Z2) is 0.8 (0.5) for multiples (singles). The p-values for the other detectors are stated in the text.

Differences in ionization energy between Ba and WIMP-search data in the ER band may result in systematic effects. Figure 5 compares the ionization-energy spectra inside the ER band. Again, KS-test p-values indicate that the Ba and WIMP-search spectral shapes are compatible (for both singles and multiples). The individual detectors (in the same order) have KS p-values of 0.2 (0.6), 0.02 (0.2), 0.7 (0.5), 0.8 (0.9) for multiples (singles), respectively. This provides assurance that any ionization-yield differences between the two data types have minimal influence on the modeling of the gamma background in the ER band. The normalizations in Figs. 3, 4 and 5 were scaled individually, and we tested only the shapes of the spectra and not their overall normalizations.

C. The surface-event background

Surface events are defined as particle interactions that occur within a few μm of the surface of a detector. Such events can have diminished charge collection and can even result in a complete loss of the ionization signal, in which case they are called zero-charge (ZC) events. The majority of surface events come from decays of the ^{210}Pb decay chain, a long-lived product of the ubiquitous ^{222}Rn whose daughters implant into surfaces during fabrication of the detectors and housings [15]. The ^{210}Pb decay chain produces relatively low-energy decay products that do not penetrate the detectors deeply enough to have full charge collection, leading to a significant number of surface or ZC events.

D. The surface-event model

We start our GEANT4 [16] simulation of the surface-event background by contaminating the surface of both the Cu detector housings and the Ge detectors with ^{214}Po nuclei that are allowed to decay isotropically [15,17]. In addition to using the standard GEANT4 physics lists it is imperative

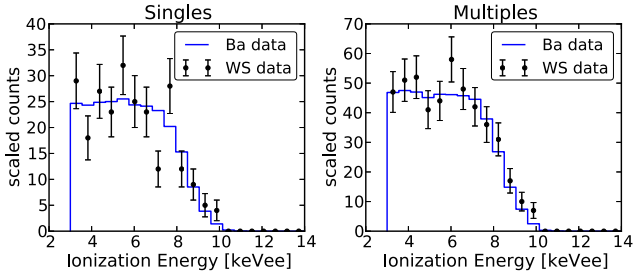

FIG. 5 (color online). Comparison of the ionization-energy spectra for events in the ER band. The singles spectrum is shown in the left panel while the multiples spectrum is shown in the right panel. Ba calibration and WS data are well matched. The p-value from a Kolmogorov-Smirnov test for the detector shown (T1Z2) is 0.2 (0.6) for multiples (singles). The p-values for the other detectors are stated in the text. The phonon energy range restriction of 3–14 keVnr effectively removes all events above 10 keVee, as seen in Fig. 1.

that the "Screened Nuclear Recoil Physics List" (SNRPL) [15,17,18] is invoked in order to correctly simulate implantation of heavy, low-energy ($\lesssim$500 keV) nuclei. The SNRPL is based on algorithms used in Stopping and Range of Ions in Matter [19] and has been confirmed to produce compatible results [18]. After the initial implantation of the ^{210}Pb nuclei, we simulate the full ^{210}Pb decay chain shown in Fig. 6. The initial ^{210}Pb decay produces a mix of electrons and low-energy photons, most of which are sufficiently low in energy to be classified as surface events [15,17]. The ^{210}Bi beta decay has an endpoint of ~1.2 MeV. In this analysis we focus on low-energy events (below ~14 keV) and therefore only a small fraction of ^{210}Bi decays will fall into our signal region, making the ^{210}Bi a subdominant component. The final decay in the ^{210}Pb decay chain is another Po-isotope alpha decay; ^{210}Po decays to ^{206}Pb, producing a 5.3 MeV alpha particle. The alpha particle is unlikely to contribute to our background because of its high energy. The 103 keV recoil energy of the ^{206}Pb nucleus, however, may be degraded sufficiently to appear in the low-energy signal region because it may have to travel some distance through the surface in which the parent ^{210}Po atom is implanted [15,17]. The number of particles produced in this decay chain is proportional to the number of alpha particles produced in the ^{210}Po decay, so the observed ^{210}Po alpha rate (measured from a high-energy sideband in the WIMP-search data) is used to estimate the total number of events expected to be observed from ^{210}Pb decay-chain products (in the low-energy signal region) for each detector.

As described above, GEANT4 [16] is utilized to simulate the particle interactions in our detectors. However, the standard GEANT4 framework is currently not capable of simulating the phonons and electron-hole pairs produced by particle interactions in semiconductor crystals (i.e., the detailed detector response), and therefore this estimation must be made after the GEANT4 simulation completes. We extended the GEANT4 framework to include these processes [20], however we did not use this new software here since it would have gone beyond the scope of this paper. The amount of phonon and ionization energy collected by

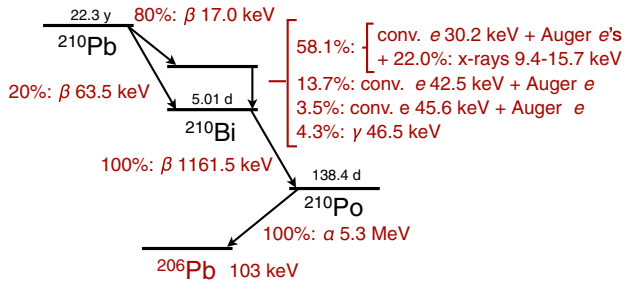

FIG. 6 (color online). The dominant decay modes of the ^{210}Pb decay chain. The alpha decay concluding this decay chain gives the ^{206}Pb nucleus 103 keV of recoil energy.

the sensors is also not modeled with GEANT4 and must be done post-simulation. Consider a particle interaction that produces an initial combination of phonons and electron-hole pairs. The phonons diffuse through the crystal, and the electron-hole pairs are drifted to the sensors using a small drift field (~3 V/cm), emitting additional phonons on the way [5]. The amount of charge collected depends on a few factors. The first (and most obvious) is the absolute number of electron-hole pairs produced by an event. For events producing recoiling electrons (from incident photons and electrons), one electron-hole pair escapes the interaction region per 3.0 eV of deposited recoil energy (on average) [21]. Events recoiling off nuclei produce fewer charge carriers, with the amount given approximately by standard Lindhard theory [4,22]. The total phonon signal is the sum of the primary phonons produced initially by the particle interaction and the Luke phonons [5] produced by the drifting charge carriers. Charge carriers that get trapped near the interaction site do not produce an ionization signal or a Luke phonon signal and therefore must be taken into account. In particular a particle hitting a detector near a surface (within ~1 μm) will have suppressed charge collection due to charge trapping [23]. In Sec. V we show evidence that for the detector sidewalls this depth scale is likely a factor of 5 smaller than for the detector faces. This led us to systematically vary the sidewall surface depth in the limit calculation presented in Sec. VI to account for systematic uncertainties. For an event that occurs further than ~1 μm away from a surface most of the produced charge is collected. For events on the side instrumented for phonon readout (henceforth referred to as the "phonon side") or on a sidewall we model the amount of charge collected to exponentially go to zero at the surface, while for events on the side instrumented for ionization readout (henceforth referred to as the "ionization side") we collect a minimum of ~50% of the produced charge carriers, exponentially increasing to 100% with a characteristic length of 1 μm (see Sec. V). Considering that the ionization and phonon sides of the detectors have different charge collection characteristics, it is possible to separate the simulation into the five components shown in Fig. 2: (1) events that originate in the Cu housings (Housing), (2) events that originate on the detector currently being studied, on either the charge side (Q-same) or (3) the phonon side (P-same). Events can also originate either from (4) the detector adjacent to the charge side (Q-opposite), or (5) the detector adjacent to the phonon side (P-opposite). We use the output from the GEANT4 simulation, taking into account the factors discussed in this section, and estimate the total amount of ionization and phonon energy for each simulated event. Figure 7 shows the result of this calculation and how the components discussed contribute to the overall event distribution in the ionization- versus recoil-energy plane. To obtain a more realistic detector response, electronic noise (as measured with calibration

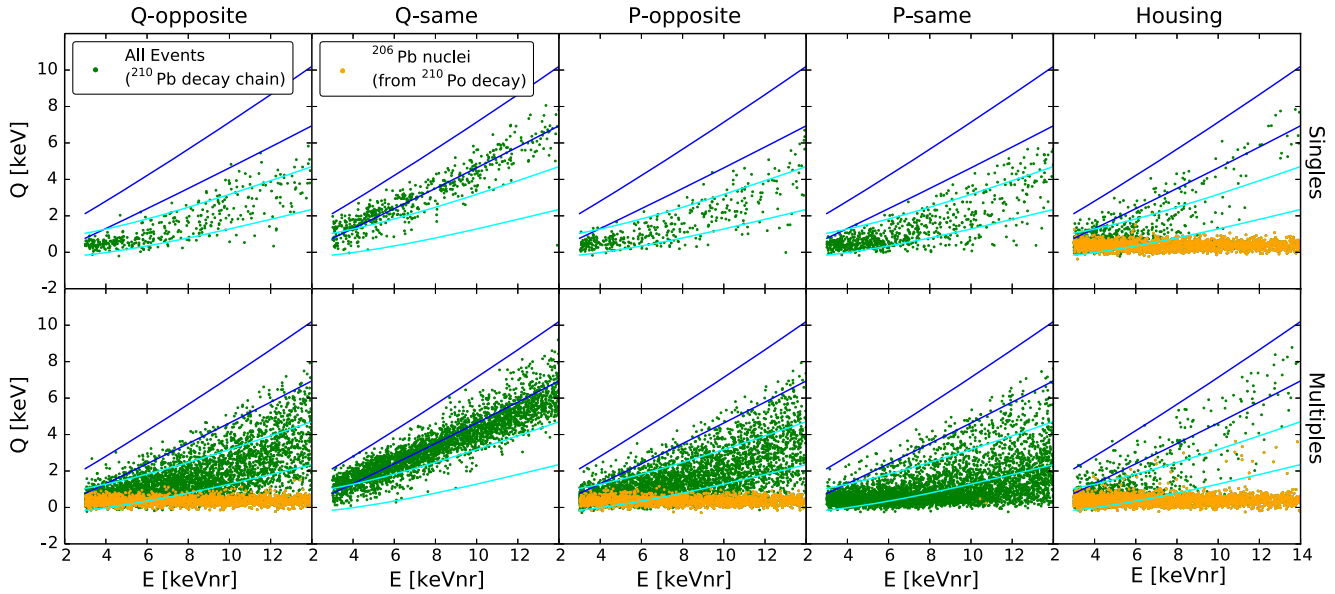

FIG. 7 (color online). Expected distribution of background events in the plane of ionization versus recoil energy (for a generic CDMS II Ge detector), from simulations of surface events originating from the adjacent detector and striking the detector's charge side (far left column), from the detector's charge side (second column from left), from the adjacent detector and striking the detector's phonon side (third column), from the detector's phonon side (fourth column), and from the housing (last column), as labeled (see Fig. 2 for a schematic). The top row shows single-scatter events and the bottom shows multiple-scatter events. The upper dark (blue) pair of curves represents the electron recoil band while the nuclear recoil band is shown by the lower, lighter (teal) pair of curves. Events from ^{210}Po decays that produce nuclear recoils are highlighted in a lighter shade (orange) at Q near zero. This simulation has ~100× more events than expected in the WIMP-search data. Note that the relative numbers of events in each plot are fixed here; none of the relative normalizations (either of the 5 components or of singles to multiples) are allowed to float. Furthermore, note that decays on different surfaces cause quite different spectra, which need to be considered for a reliable background model.

data) was added to the simulated ionization and phonon energies.

E. The full background model

The gamma background is straightforwardly modeled with Ba calibration events. The surface-event background is more difficult due to uncertainty in the locations of the radio contaminants, which are only partially constrained by the observed ^{210}Po alpha decays. Figure 8 shows energy histograms of the observed alpha events that produced most of their ionization signal in the inner sensor (detector face) and on the outer sensor (housing). Unfortunately, uncertainties on the observed alpha rates are large because saturation effects make it difficult to reliably reconstruct events at such high energies, and because CDMS II detectors, in contrast to SuperCDMS iZIPs [17], cannot reliably determine whether an event occurred on the top or the bottom of a detector. We construct the surface-event component of the detector-face background model by assuming that 1/4 of the contamination is on each of the four flat surfaces: the detector's top and bottom and the facing sides of the adjacent detectors. Consequently, the number of simulated primaries from each detector face is equal. The number of events expected from the detector housings can be constrained by counting the number of alpha events that are identified as events occurring on the outer wall of a detector. Hence the 5 components discussed at the end of Sec. III D and in Fig. 7 are reduced to a "housing" and a "detector-face" component. In the ML fit

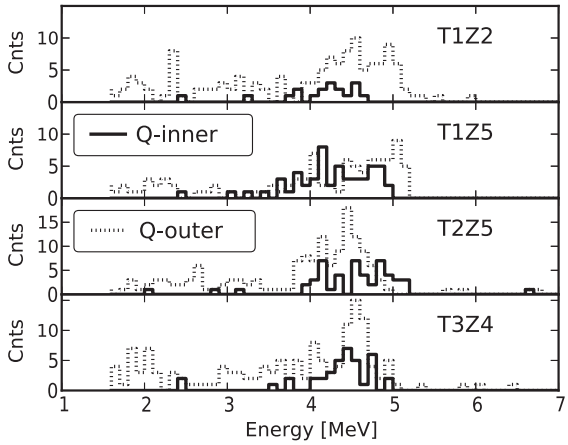

FIG. 8. Spectra of alpha events observed in (from top to bottom) detector T1Z2, T1Z5, T2Z5, and T3Z4. Our analysis assumes that any alpha with energy > 4 MeV is from a ^{210}Po decay. Shown are alpha events detected on the inner ("Q-inner," solid) and outer ("Q-outer," dashed) electrodes. Q-outer events most likely originate from the copper housings.

the relative normalization of the different components is fixed accordingly.

IV. MAXIMUM LIKELIHOOD ANALYSIS

Based on the surface-event simulations and gamma-background estimates obtained from Ba calibrations, we perform a maximum likelihood analysis to extract the number of WIMP-like events in the WIMP-search data. We assume each event in the sample is one of three species: ER, SE, or NR. The probability density function (PDF) for each species as a function of phonon energy p and ionization energy q is denoted as $\mathcal{P}_{XX}(p,q)$. $\mathcal{P}_{\mathrm{SE}}(p,q)$ is constructed from the surface-event simulation to be further discussed in Sec. V, $\mathcal{P}_{\mathrm{ER}}(p,q)$ is constructed from Ba calibration data, and $\mathcal{P}_{\mathrm{NR}}(p,q)$ is constructed from a simulated WIMP component at a specific WIMP mass with the ionization yield of each event determined from Lindhard theory. All PDFs are two-dimensional binned histograms. The NR PDFs are included for both singles and multiples data; since the multiples data cannot include a real WIMP signal, including the NR PDF in the multiples data provides a useful check for a systematic mischaracterization of a background that might result in an apparent WIMP signal in the singles. In the fits, the NR component is either set identically to zero or allowed to float.

The fitting is performed using a two-dimensional extended likelihood function

$$\mathcal{L} \equiv e^{-\bar{N}} \prod_{i}^{N} (N_{\mathrm{ER}}\mathcal{P}_{\mathrm{ER},i} + N_{\mathrm{SE}}\mathcal{P}_{\mathrm{SE},i} + N_{\mathrm{NR}}\mathcal{P}_{\mathrm{NR},i}) \quad (1)$$

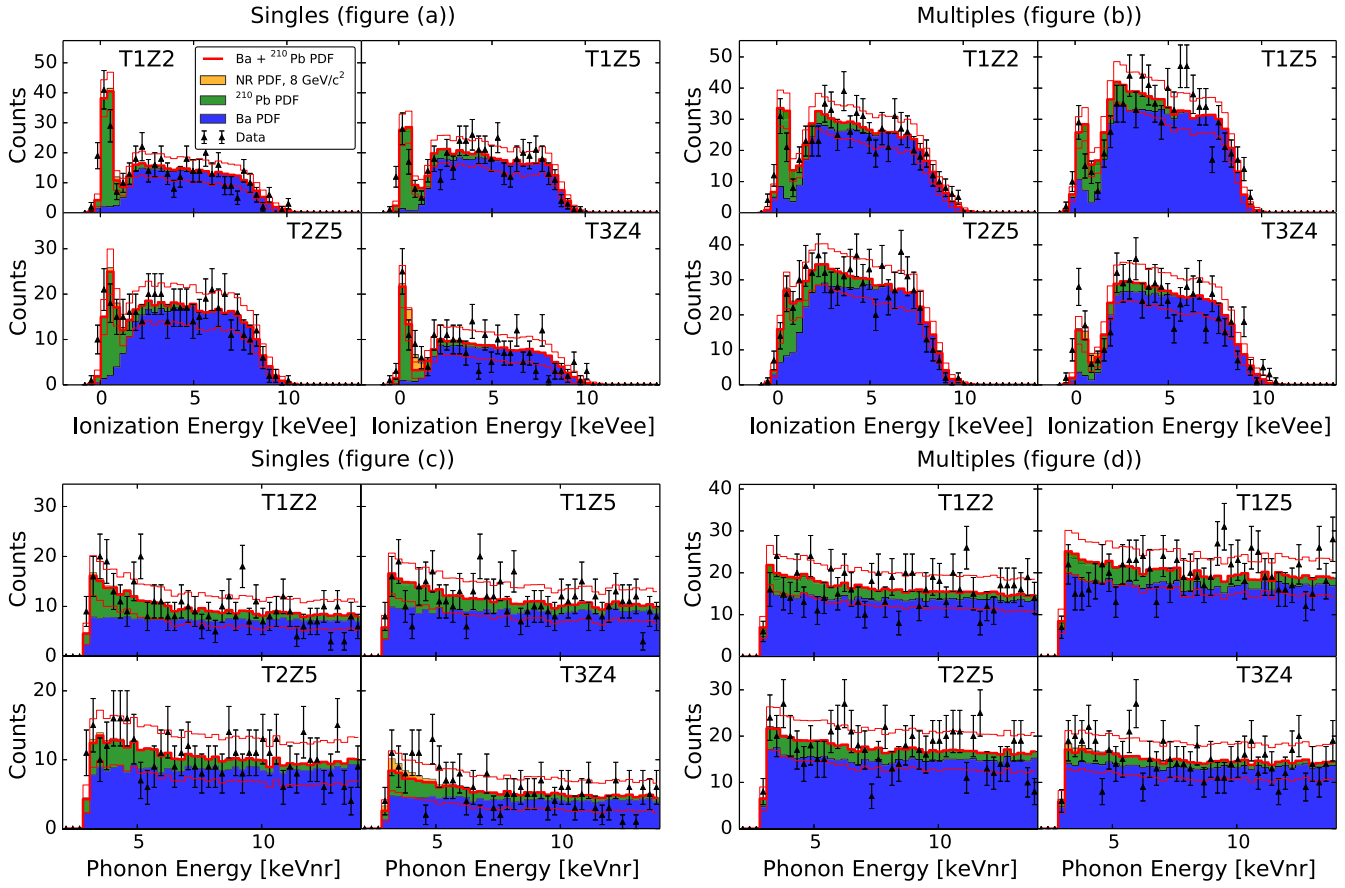

FIG. 9 (color online). Stacked histograms of either phonon or ionization energy. Figures (a) and (c) show the ML best-fit result to WIMP-search data singles, while Figs. (b) and (d) show the ML best fit to WIMP-search data multiples. Figures (a) and (b) show the projection in ionization energy while (c) and (d) show the projection in phonon energy. The four canvases in each figure show the result for each of the four detectors. The combined components of the surface-event background model are represented by the solid green histogram (legend title: ^{210}Pb PDF), while the gamma-background model is shown in blue (legend title: Ba PDF). The combined probability density functions from simulation and calibration data are shown as the thick line on top of the solid histograms (the thin lines indicate the statistical uncertainties), while the WIMP-search data are shown in black error bars. The orange histogram (legend title: NR PDF) represents the best-fit nuclear recoil-like component. The agreement is good, with T3Z4 having the worst fit of the four detectors caused by two histogram bins after the low-energy peak [Figs. (a) and (b)] which are not fit well. The low-energy peak of that detector in the multiples is also not fit well, which may be a result of miscalibration due to a lack of penetration-depth calibration data for this detector.

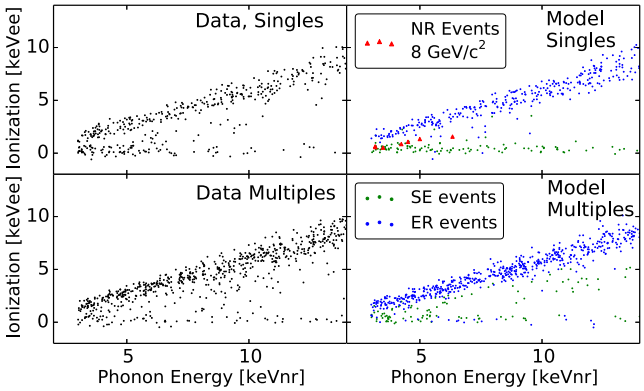

FIG. 10 (color online). A comparison between WIMP-search data (left column) and the background model (right column) for one detector (T1Z2), with a NR component representative of an 8 GeV/c^2 WIMP shown with the background-model singles. The number of points displayed for the background model has been reduced to match the number in the WIMP-search data. The likelihood fit is performed in this two-dimensional space of ionization versus phonon energy.

where N is the total number of events entering the fit, N_{XX} is the fitted number of events per species, and $\bar{N} \equiv N_{\mathrm{ER}} + N_{\mathrm{SE}} + N_{\mathrm{NR}}$ is the total number of fitted events. $\mathcal{P}_{XX,i}$ is equivalent to $\mathcal{P}_{XX}(p_i, q_i)$ with p_i and q_i representing the phonon and ionization signal for each event respectively. The only free parameters in the fits are N_{ER}, N_{SE}, and (when applicable) N_{NR}. Note that the relative contributions to the SE PDF (shown in Fig. 7) are fixed; only the total number of SE events is allowed to float. Furthermore, singles and multiples data are fit independently for each detector.

The result is shown in Fig. 9, with the best-fit combined PDF shown as the top of the solid histograms for each detector, while low-energy WIMP-search data are shown as points with error bars. Figure 10 compares WIMP-search data with the background model in the two-dimensional space in which fits are performed. The number of simulated events displayed in Fig. 10 has been reduced to be representative of the best-fit value.

V. SYSTEMATICS

The fits done in Sec. IV and the background model described in Sec. III depend on parameters that are measured in the experiment itself in order to properly reproduce the observed data. Known systematic effects include possible inaccuracies in the near-surface ionization model (see Sec. III D) for SE, inaccuracies in the model of the noise and stability characteristics of each detector, and differences between the Ba calibration data and the low-energy WIMP-search data (see Sec. III B). For this analysis we consider uncertainty in only the near-surface ionization model because it has the greatest impact on the background model and simultaneously has the most intrinsic uncertainty.

The near-surface ionization model is based on a Monte Carlo study constrained by fits to calibration data to determine the ionization yield as a function of distance from a detector surface (or "depth"). There are two parts to this study. First, events near the surface of a detector need to be identified and segregated according to whether they are near the surface with the phonon or ionization sensors. This is done using events from ^{133}Ba calibration that have simultaneous energy depositions in the detector under study and in either the detector above or below (i.e., top or bottom surface of detector under study). Secondly, GEANT4 is used to simulate ^{133}Ba events. The simulated events can have more than one interaction within a given detector, and so combined coordinates (x, y, z) for each event are determined by computing an average of the individual scatters positions (weighted by energy). The ionization yield versus depth has been calibrated using data from the UC Berkeley test facility (during detector testing) [24]. Using this information, the recoil energy and yield are calculated for each Monte Carlo event. Near-surface events are then identified in the simulated data set using data-selection cuts equivalent to those used for the real ^{133}Ba data. The Monte Carlo events and the real ^{133}Ba events are then combined. This is accomplished by taking all data events on the chosen detector face with yield < 0.7. We make the assumption that yield versus depth is a monotonic function in both the real and simulated data. The Monte Carlo events are averaged to have the same number of entries as the real data and the two are compared. We measure the ionization yield from the real data and take the corresponding depth from the comparison with the simulated data. This enables us to extract the yield versus depth profile for each of the detectors and surfaces. This study showed some variation between detectors, but also showed that more ionization is collected for events that hit the ionization side of the detectors compared to the phonon side. The assumption is that for events that hit the ionization side of a detector at least 50% of the electron and hole pairs are collected. The collection efficiency exponentially increases to 100% with a characteristic depth scale of $\sim$1 μm. For events on the phonon side, calibration data are consistent with the assumption that no charge is collected directly at the surface. The amount of charge collected increases exponentially with the same characteristic depth as the ionization side of the detectors. The last surface is the detector sidewall. There is currently no calibration data available for the detector sidewalls. Fitting WIMP-search multiples data we find a preference for a characteristic sidewall depth $\sim$5$\times$ smaller than for the flat faces. Thus, an event hitting the detector sidewall will have a higher percentage of its charge collected than events hitting the flat surfaces.

The reduced charge collection for events near the flat surfaces is caused by the readout sensors. Hot charge

carriers can back diffuse through a 40 nm thick amorphous-Si layer into the sensors and be lost. Furthermore, charges near one of the flat surfaces will be attracted to opposite-sign image charges in the metals making up the readout sensors. For events on the sidewall, the main mechanism leading to a reduced charge signal is charge trapping. Electric field lines can terminate on the sidewall causing charges not to produce a signal in the sensor. This effect is partially compensated by the fact that a free charge near a bare Ge surface experiences a repulsive force from an image charge of the same sign.

The observed rate on the detector sidewalls is larger than on the flat surfaces because of higher contamination of the copper surfaces, so the most sensitive parameter in the model is the characteristic penetration depth into the sidewall. We focus on this parameter in our systematic error evaluation, as an exhaustive search of the full parameter space is computationally prohibitive. The resulting calculation therefore provides a minimum estimate of the systematic uncertainty. In Fig. 11 we show the best-fit likelihood ratio as a function of the assumed sidewall characteristic depth. We estimate the sidewall depth parameter from fitting multiples data, which should have no WIMP component, to the background model without a NR component. Figure 11 indicates that the model is optimized near $\sim 0.5\ \mu$m and becomes worse as the characteristic penetration depth is increased or decreased. Other parameters of the near-surface ionization model also have an impact on the fit quality, however much less so. Performing likelihood ratio tests to compare the fit qualities between different characteristic depths for the flat detector faces shows that comparing the worst fit to the best fit has a

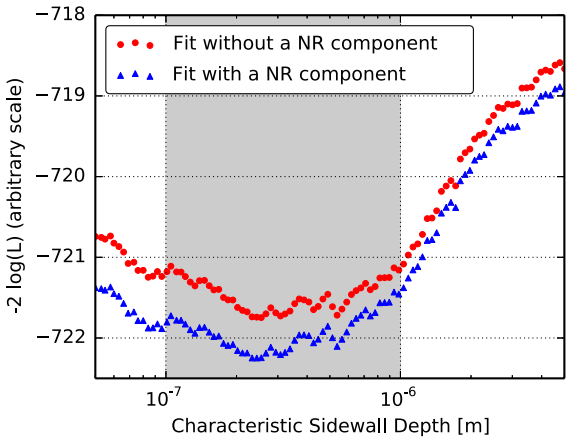

FIG. 11 (color online). The best-fit negative log-likelihood value for multiples data at various characteristic sidewall depths. A more negative value indicates a better fit, although the absolute scale is arbitrary. We show the best-fit negative log-likelihood value for both a fit with and without a nuclear recoil component. The gray shaded region is the region over which we marginalize (using a flat prior) in order to take into account this systematic in the final result.

negative log-likelihood value difference that is $\sim 5\times$ smaller than doing the equivalent comparison varying the sidewall characteristic depth parameter. Since the main focus of this work is the ML fitting technique, used by the CDMS Collaboration for the first time, we have not done an exhaustive systematic study, nor have we attempted to minimize the systematic uncertainties. In future analyses of SuperCDMS data, we plan to further reduce the systematic effects by using a detector Monte Carlo simulation [20] to more accurately simulate detector physics and thus better determine the detailed detector response. Moreover, for our new iZIP detectors, additional calibration data has already been analyzed [17], and we plan to perform experimental studies of sidewall contamination. For the analysis here, we estimate the systematic effects by varying the sidewall depth parameter between 0.1 and 1 μm (the shaded region in Fig. 11).

VI. RESULTS

Having discussed the generation of a background model based on physical knowledge of our detectors, we are now ready to compute an exclusion limit on the WIMP-nucleon cross section using the ML technique. Systematic effects need to be taken into account, and as discussed in Sec. V we assume that the uncertainty in the sidewall characteristic depth between 0.1–1 μm is a good approximation for the systematic effects encountered in this analysis.

To calculate a limit on the WIMP cross section we compared our results with the results of Monte Carlo simulations that include known numbers of WIMP scatters among the background events. These simulations generated events from background and WIMPs according to the $\mathcal{P}_{XX}$ and N_{XX} also used in defining the likelihood of Eq. (1). Before producing simulations, for each sidewall characteristic depth the maximum likelihood value and uncertainty of N_{ER} (and of N_{SE}) was found from the data with N_{NR} constrained to be zero. Then for each simulation a random value of N_{ER} (N_{SE}) was generated according to the maximum likelihood and uncertainty. This random value was in turn taken as the expectation for a Poisson random choice of N_{ER} (N_{SE}) chosen for the simulation. The simulation's N_{ER} and N_{SE} numbers of events were generated for the given sidewall characteristic depth according to the already described PDFs, $\mathcal{P}_{XX}(p, q)$. Singles data and singles PDFs were used for generating Monte Carlo (MC) background of singles, and multiples data and multiples PDFs were used for generating MC background of multiples. Singles and multiples data were fit independently and the ratio between the two was not fixed. However, we performed checks on the final, best-fit ratios to ensure that they are consistent with the initial estimates. The expectation value of N_{NR}, the number of WIMPs, depends on the Galactic halo model, the WIMP mass and cross section, and the experiment's detection efficiency, run time, and detector mass, all of which were taken from what CDMS assumed

and measured in past analyses [3,4]. Given the expectation of N_{NR}, a Poisson random number of WIMPs was chosen, and that number of WIMPs was generated according to the WIMP PDF. 20000 simulations of background plus WIMPs were produced and fit for each sidewall characteristic depth, WIMP mass, and N_{NR} expectation value.

For each WIMP mass between 5 and 20 GeV/c^2, and each sidewall characteristic depth, we began the upper limit calculation by first finding the maximum likelihood best-fit number of WIMPs in the singles data, N_{NR}. For various values of the WIMP cross section we performed 20000 MC simulations of the experiment, each with an assumed WIMP cross section, and found N_{exceed}, the number of simulations for which the maximum likelihood best-fit N_{NR} exceeded the value found in the singles data. In Fig. 12 the black curve indicating the 90% upper limit for each WIMP mass shows the cross section for which 90% of MC simulations found at least as many events as were found in the real data. In order to include a crude estimate of the effect of systematics, we marginalized over sidewall characteristic depth. The calculation of N_{exceed} was done for each sidewall characteristic depth, and the resulting values were summed over 50 uniformly spaced sidewall characteristic depths from 0.1–1.0 μm. The 90% upper limit for the WIMP mass under consideration was then taken to be the cross section for which this total sum of the N_{exceed} values was at least 90% of the total number of MC simulations over all characteristic sidewall depths. This procedure weakens the limit, because for large sidewall depths ($\sim$1 μm) the ML fit number of WIMPs from the data increases significantly and dominates the limit.

A 90% sensitivity curve was also computed. To obtain the dashed (red) curve in Fig. 12 a calculation was done similar to that for the 90% upper limit, but with the singles data value of N_{NR} replaced by values found from fits to MC simulations generated without WIMPs. Since the MC fit values of N_{NR} vary from one simulation to another, the 90% upper limits vary. This variation is indicated by 1σ and 90% regions about the sensitivity curve (darker and lighter green bands).

In order to test our methods on data that we know are free of WIMPs, the upper limit and sensitivity results were also calculated from multiples data treated as if WIMPs could be present. The sensitivity and limit are shown in Fig. 12.

The limit at low WIMP masses is stronger than the expected sensitivity, while at high WIMP masses it is weaker. The fact that the limit is above the 90% sensitivity band (the light green band in Fig. 12) points to either a possible WIMP signal (if limits set by other experiments are not taken into consideration) or more likely a deficiency in the background model. The WIMP significance above 10 GeV/c^2 is $\sim 2\sigma$. In order to check the background model we can also produce a limit plot using multiples data instead of singles data. Of course multiples data do not contain any WIMP signal, and therefore the sensitivity should agree with the limit within statistical fluctuations for a perfect background model. This is shown in Fig. 12 in the right panel. While there does not appear to be a fluctuation to a stronger than expected limit at low WIMP masses, the trend seen in the singles limit of a weaker limit at higher WIMP masses is repeated in the multiples data. This result suggests that small residual systematics in the background

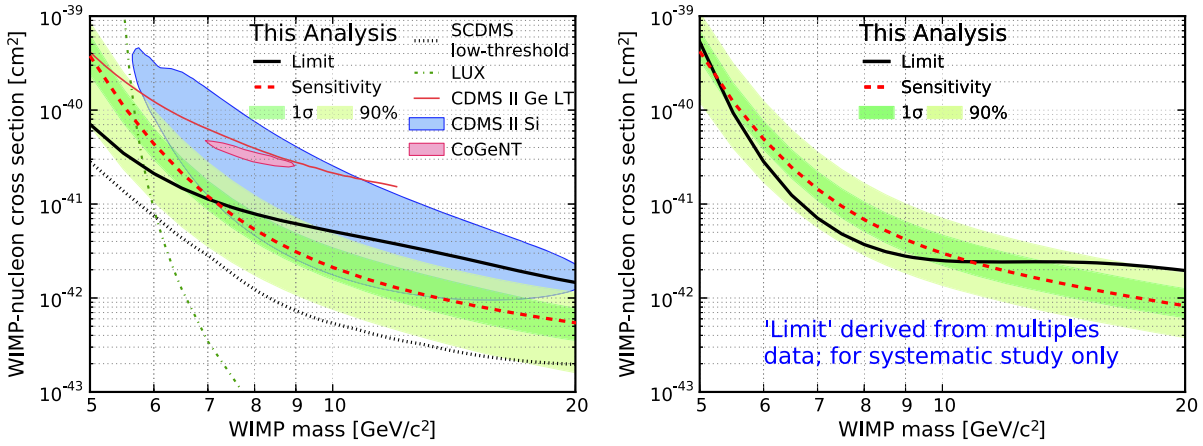

FIG. 12 (color online). Left panel: The limit (with standard halo assumptions and standard nuclear form factors as used in [4,10,11]) computed for this analysis is shown as the thick solid black line. The thick, dashed (dark-red) line is our best estimate for the expected sensitivity of this analysis, with the green (light-green) shaded region directly around it indicating the 1σ (90%) uncertainty. The limit is stronger than the estimated sensitivity below $\sim$7 GeV/c^2, while at larger WIMP masses the limit is systematically above the sensitivity, indicating a systematic effect not yet taken into account. Right panel: This figure shows the limit calculated using multiples data instead of singles data. Multiples data do not contain WIMPs, and therefore the expected sensitivity and the limit should be identical to within statistical fluctuations. A similar trend of a stronger than expected limit at lower WIMP masses and a weaker than expected limit at higher masses is observed, indicating that the same systematic effect that is present in the singles is also present in the multiples data, although to a lesser extent.

model are responsible for weakening the limit for higher WIMP masses.

The power of performing a likelihood analysis is illustrated in Fig. 12 by comparing the "CDMS II LT" curve, based on analysis of the same data without background subtraction [4], to the limit of this analysis. We see a factor of ~5 improvement. Another check of the power of a likelihood analysis is to compare the sensitivity of this analysis to the sensitivity of the SuperCDMS low-threshold result [25]. Both analyses are background limited, but the background in the CDMS II data analyzed here is considerably higher than the background in the SuperCDMS data. However, with the advanced analysis technique presented here we reach a sensitivity that almost scales with the exposure (for a 4.5 times larger exposure, SuperCDMS increases the sensitivity by a factor of 5). This result suggests that the technique presented here may help to improve current SuperCDMS limits, as well as those of future experiments.

VII. COMPARISONS TO THE COLLAR-FIELDS STYLE FITS

For comparison, we also perform a maximum likelihood fit to the WIMP-search data using analytic PDFs similar to those used by Collar and Fields [12]. The form of the likelihood function is similar to Eq. (1) except the three components are ER, ZC, and NR explicitly written as

$$\mathcal{L} \equiv e^{-\bar{N}} \prod_{i}^{N} (N_{\mathrm{ER}} \mathcal{P}_{\mathrm{ER},i} + N_{\mathrm{ZC}} \mathcal{P}_{\mathrm{ZC},i} + N_{\mathrm{NR}} \mathcal{P}_{\mathrm{NR},i}). \quad (2)$$

Instead of using histograms the PDFs are two-dimensional functions in (q, p). Specifically, the PDFs are of the form:

$$\mathcal{P}_{XX}(q,p) = \exp(-A_{2,XX}p) \exp\left(\frac{-(q - C_{XX}(p))^2}{S_1^2 + S_2 C_{XX}(p)}\right), \quad (3)$$

where C_{XX} is a polynomial describing the mean q of the recoil band as a function of p. We use a polynomial of order 0 (1,2) for the ZC (ER, NR) band, respectively. For the fit to the data from individual detectors, the coefficients C_{XX} are fixed to values obtained from calibration samples from that detector. We also perform fits to the singles and multiples samples where we combine data from all of the detectors; in these fits the C_{XX} are allowed to float. Following [12], the ER PDF is slightly modified from Eq. (3) to include surface events with incomplete charge collection (the so-called "Crystal Ball" function [26]). Note that this treatment is different from the model described in Sec. III E where the events with zero and incomplete charge collection are included in the same PDF. The results of the fits using the analytic PDFs are summarized in Table I. They are in reasonable agreement with Ref. [12] considering there are some differences in the data sets used. In particular, we observe a significant improvement (4.4σ) to the fit to singles data when a NR component is included. However, we also see a significant improvement (5.2σ) when we perform these fits to the multiples data (also shown in Table I).

In addition, we performed fits using the analytic model to an ensemble of toy MC data sets generated from the best fit of our background model (without a NR component) to the

TABLE I. The number of NR-like events and the NR exponential constant extracted from the WIMP-search data using the analytic fit (described in the text). We also provide the equivalent numbers from [12]. The "simulation" columns show what happens if we fit our background model using the Collar-Fields PDFs defined in Eq. (3). The observed excess in this case is on par with the observed excess in WIMP-search data. The last two columns (labeled "Likelihood") show the number of WIMP-like events preferred (for a mass of 8 GeV/c^2) when WIMP-search data are fit with our background model using a sidewall depth of 0.3 μm (the optimal value, see Fig. 11). We chose a mass of 8 GeV/c^2 because that is the preferred value for the Collar-Fields-type analysis, as well as other closed contours (see Fig. 12). Using our background model we do not observe an excess at this WIMP mass (see last 2 columns).

	Collar & Fields [12]		CDMS Collaboration Analyses									
	Singles		Singles data		Multiples data		Singles simulation		Multiples simulation		Likelihood	
Detector	N_{NR}	A_2	N_{NR}	A_2	N_{NR}	A_2	N_{NR}	A_2	N_{NR}	A_2	Singles	Multiples
T1Z2	33 ± 9	0.6 ± 0.1	23 ± 8	0.4 ± 0.1	10 ± 6	1.5 ± 0.7	22 ± 9	0.7 ± 0.3	7 ± 10	0.9 ± 0.7	8 ± 13	-7 ± 10
T1Z5	18 ± 6	0.7 ± 0.3	16 ± 6	0.5 ± 0.2	17 ± 8	0.2 ± 0.2	13 ± 8	0.7 ± 0.4	11 ± 10	0.9 ± 0.6	-1 ± 11	-7 ± 11
T2Z3	37 ± 19	0.7 ± 0.2	30 ± 18	0.9 ± 0.4	45 ± 13	0.5 ± 0.2						
T2Z5	26 ± 14	0.8 ± 0.4	30 ± 13	0.9 ± 0.4	83 ± 16	0.4 ± 0.1	30 ± 9	0.7 ± 0.3	32 ± 11	0.8 ± 0.3	6 ± 18	2 ± 20
T3Z2	26 ± 10	0.7 ± 0.2	14 ± 12	1.1 ± 0.7	17 ± 12	0.5 ± 0.4						
T3Z4	12 ± 4	0.6 ± 0.2	10 ± 4	0.6 ± 0.2	8 ± 5	0.6 ± 0.4	5 ± 5	0.9 ± 0.5	6 ± 7	0.9 ± 0.6	9 ± 13	6 ± 13
T3Z5	4 ± 10	2.0 ± 2.4	9 ± 10	1.8 ± 1.2	91 ± 18	0.4 ± 0.1						
T3Z6	22 ± 11	0.7 ± 0.4	24 ± 8	0.6 ± 0.3	2 ± 3	0.0 ± 0.1						
Best four	89 ± 18		79 ± 17		118 ± 20		72 ± 13	0.6 ± 0.1	68 ± 16	0.7 ± 0.2	22 ± 28	-6 ± 29
All dets	178 ± 32	0.7 ± 0.1	153 ± 33	0.6 ± 0.1	231 ± 34	0.6 ± 0.1	72 ± 13	0.6 ± 0.1	68 ± 16	0.7 ± 0.2	22 ± 28	-6 ± 29

WIMP-search data (as detailed in Sec. VI). The average fitted number of NR events and $A_{2,\mathrm{NR}}$ (from 100 data sets) are shown in the columns of Table I, labeled "Singles simulation" and "Multiples simulation." We see good agreement when comparing the fitted WIMP parameters between these toy (WIMP-free) data sets and the fits to data. These two factors, significant WIMP components in the multiples data and in toy data sets generated from our physics-based model (without a NR component), lead us to conclude that the excess NR-like events identified by the Collar-Fields analytical model are not true nuclear recoils but are instead due to an inability of this parametrization to adequately describe the background. Finally, the Table I columns labeled "Likelihood" show results of fits to WIMP-search data using our background model plus an 8 GeV/c^2 WIMP component. There are $<1\sigma$ WIMP-like upward (downward) fluctuations in singles (multiples) data. It is clear that our background model performs significantly better than the *ad hoc* parametrization from [12]. We believe the superiority of our background model can be attributed to the inability of the *ad hoc* functions to properly describe the surface-event background from the ^{210}Pb decay chain.

VIII. CONCLUSION

We presented the results of a maximum likelihood fit to the low-energy CDMS II Ge WIMP-search data. We used a background model derived from detector simulations and calibrations from the known contributing sources. We observe no significant NR component in our data and set a limit on the WIMP-nucleon cross section as a function of WIMP mass that is generally 5× stronger than our previous analysis of these data, which did not include any background subtraction [4]. This result demonstrates the power of the ML technique for low-threshold WIMP searches. We also performed a fit to the data set using the *ad hoc* analytic PDFs suggested by Collar and Fields [12], that produces a significant excess of NR-like events in this data set. Using their method, we reproduce their results for the single-scatter data but also observe a significant excess in multiple-scatter data, leading us to conclude that their analytical model is insufficient to describe the backgrounds.

ACKNOWLEDGMENTS

The CDMS Collaboration gratefully acknowledges the contributions of numerous engineers and technicians; we would like to especially thank Dennis Seitz, Jim Beaty, Bruce Hines, Larry Novak, Richard Schmitt, Astrid Tomada, and John Emes. In addition, we gratefully acknowledge assistance from the staff of the Soudan Underground Laboratory and the Minnesota Department of Natural Resources. This work is supported in part by the National Science Foundation, by the United States Department of Energy, by NSERC Canada, and by MultiDark (Spanish MINECO). Fermilab is operated by the Fermi Research Alliance, LLC under Contract No. De-AC02-07CH11359. SLAC is operated under Contract No. DE-AC02-76SF00515 with the United States Department of Energy.

[1] P. A. R. Ade *et al.* (Planck Collaboration), Planck 2013 results. I. Overview of products and scientific results, Astron. Astrophys. **571**, A1 (2014).
[2] G. Steigman and M. Turner, Cosmological constraints on the properties of weakly interacting massive particles, Nucl. Phys. **B253**, 375 (1985).
[3] D. S. Akerib *et al.*, Low-threshold analysis of CDMS shallow-site data, Phys. Rev. D **82**, 122004 (2010).
[4] Z. Ahmed *et al.*, Results from a Low-Energy Analysis of the CDMS II Germanium Data, Phys. Rev. Lett. **106**, 131302 (2011).
[5] P. N. Luke, Voltage assisted calorimetric ionization detector, Appl. Phys. Lett. **64**, 6858 (1988).
[6] R. Bernabei *et al.*, First results from DAMA/LIBRA and the combined results with DAMA/NaI, Eur. Phys. J. C **56**, 333 (2008).
[7] C. E. Aalseth *et al.*, Search for an Annual Modulation in a *p*-Type Point Contact Germanium Dark Matter Detector, Phys. Rev. Lett. **107**, 141301 (2011).
[8] R. Agnese *et al.*, Silicon Detector Dark Matter Results from the Final Exposure of CDMS II, Phys. Rev. Lett. **111**, 251301 (2013).
[9] Z. Ahmed *et al.*, Search for annual modulation in low-energy CDMS II data, arXiv:1203.1309.
[10] R. Agnese *et al.*, CDMSlite: A Search for Low-Mass WIMPs using Voltage-Assisted Calorimetric Ionization Detection in the SuperCDMS Experiment, Phys. Rev. Lett. **112**, 041302 (2014).
[11] D. Akerib *et al.*, First Results from the LUX Dark Matter Experiment at the Sanford Underground Research Facility, Phys. Rev. Lett. **112**, 091303 (2014).
[12] J. I. Collar and N. E. Fields, A maximum likelihood analysis of low-energy CDMS data, arXiv:1204.3559.
[13] D. Akerib *et al.*, Exclusion limits on the WIMP-nucleon cross section from the first run of the Cryogenic Dark Matter Search in the Soudan Underground Laboratory, Phys. Rev. D **72**, 052009 (2005).
[14] M. A. Stephens, Edf statistics for goodness of fit and some comparisons, J. Am. Stat. Assoc. **69**, 730 (1974).

[15] P. Redl, Accurate Simulations of ^{206}Pb Recoils in SuperCDMS, J. Low Temp. Phys. **176**, 937 (2014).
[16] J. Allison *et al.*, Geant4 developments and applications, IEEE Trans. Nucl. Sci. **53**, 270 (2006).
[17] R. Agnese *et al.*, Demonstration of surface electron rejection with interleaved germanium detectors for dark matter searches, Appl. Phys. Lett. **103**, 164105 (2013).
[18] M. H. Mendenhall and R. A. Weller, An algorithm for computing screened Coulomb scattering in GEANT4, Nucl. Instrum. Methods Phys. Res., Sect. B **227**, 420 (2005).
[19] J. F. Ziegler, M. D. Ziegler, and J. P. Biersack, SRIM—The stopping and range of ions in matter, Nucl. Instrum. Methods Phys. Res., Sect. B **268**, 1818 (2010).
[20] D. Brandt, R. Agnese, P. Redl, K. Schneck, M. Asai, M. Kelsey, D. Faiez, E. Bagli, B. Cabrera, R. Partridge, T. Saab, and B. Sadoulet, Semiconductor phonon and charge transport Monte Carlo simulation using Geant4, arXiv:1403.4984.
[21] X.-F. Navick, M. Chapellier, F. Déliot, S. Hervé, and L. Miramonti, 320 g ionization-heat bolometers design for the EDELWEISS experiment, Nucl. Instrum. Methods Phys. Res., Sect. A **444**, 361 (2000).
[22] P. Smith and J. Lewin, Dark matter detection, Phys. Rep. **187**, 203 (1990).
[23] V. Mandic *et al.*, Study of the dead layer in germanium for the CDMS detectors, Nucl. Instrum. Methods Phys. Res., Sect. A **520**, 171 (2004).
[24] T. Shutt, M. Kesden, S. Golwala, J. Emes, J. Hellmig, B. Sadoulet, and B. Young, Charge collection and electrode structures in ionization and phonon based dark matter detectors, AIP Conf. Proc. **605**, 513 (2002).
[25] R. Agnese *et al.*, Search for Low-Mass WIMPs with SuperCDMS, Phys. Rev. Lett. **112**, 241302 (2014).
[26] M. Oreglia, Ph.D. thesis, SLAC, Stanford University, 1980.